Astron. Astrophys. 326, 366–372 (1997)

ASTRONOMY
AND
ASTROPHYSICS

HCO^+ (J = 4−3) mapping of the molecular disk around IRS 7 in Corona Australis⋆

I.M. Anderson[1], **J. Harju**[1], **and L.K. Haikala**[1,2]

[1] Observatory, P.O. Box 14, FIN-00014 University of Helsinki, Finland
[2] Swedish-ESO Submillimetre Telescope, European Southern Observatory, Casilla 19001 Santiago 19, Chile

Received 24 December 1996 / Accepted 24 April 1997

Abstract. Submillimetre $HCO^+(J = 4 - 3)$ mapping observations of the immediate environs of the infrared source IRS 7 in Corona Australis have provided corroborative evidence for the existence of the rotating molecular disk detailed in our earlier paper. An improved estimate of $0.8\,M_\odot$ for the mass of the central protostar is obtained.

Key words: stars: formation – stars: individual: R CrA IRS 7 – ISM: jets and outflows – ISM: kinematics and dynamics – radio lines: ISM

1. Introduction

Anderson et al. (1996, hereafter Paper I) detected a large molecular disk around the protostellar object IRS 7 in Corona Australis. Also revealed were a dense, bipolar molecular outflow originating from close by IRS 7 plus a dense, quiescent core located in the disk's foreground. The observations indicate that the blueshifted lobe of the bipolar outflow is interacting with the foreground core. The authors further suggested that the disk system is accreting material from the foreground core.

The disk's morphology and the mass of central protostellar object were derived from $HCO^+(J = 3-2)$ and $C^{18}O(J = 2-1)$ 1.3 mm observations conducted with the 15-m Swedish-ESO Submillimetre Telescope (SEST). Although the disk is large with a major axis length in excess of 6 000 AU, corresponding to $46''$ at the cloud's distance 130 pc, it was only marginally resolved along its major axis and unresolved along its minor axis leading to uncertainties in the derived disk parameters.

From its mid to near-IR spectral energy distribution (Wilking et al. 1986), IRS 7 has, adopting the definition given by Lada (1987), an IR spectral index of ~ 3. According to this classification scheme IRS 7 can thus be categorized as a Class I source: a deeply embedded, evolved protostar which has already accreted much of its final stellar mass (André & Montmerle, 1994). Recent ASCA satellite X-ray observations over an energy range $0.5 - 10$ k eV by Koyama et al. (1996) and centred on the Coronet cluster (Taylor & Storey, 1984) have yielded some intriguing results. IRS 7 is identified as the likely source of the hardest and most intense ($L[0.5 - 10\,\mathrm{k\,eV}] = 1.17 \times 10^{31}\,\mathrm{erg\,s^{-1}}$) X-ray emission in the region. Furthermore, the X-ray flux from this source was observed to increase by at least a factor of 3 during a flaring event which lasted for some 5 days. The positive identification of a Class I protostar as a hard X-ray source is significant: Although Class II and III objects, corresponding respectively to embedded and naked T Tauri stars, are thought to radiate X-rays as a result of enhanced, solar-like magnetic field activity no convincing explanation has yet been formulated to account for the X-ray emission from younger Class I sources. Proposed solutions include nonmagnetic heating by accretion shocks (Casanova et al. 1995) and increased protostellar magnetic field activity. Whether these magnetic fields are produced by the dynamo mechanism or whether they can be identified with fossil fields from the progenitor molecular cloud is uncertain (Montmerle et al. 1993).

Continuing from the previous work presented in Paper I, we have mapped the disk and its vicinity in the $J = 4 - 3$ transition of the formyl ion, HCO^+, at 0.8 mm using the SEST. The purpose of these observations was to elicit higher spatial resolution data on the velocity structure of the disk and, thereby, to improve upon our earlier estimate for the mass of the central protostar.

The plan of the paper is as follows: In Sect. 2 we describe the observations and in Sect. 3 we discuss the analysis of the data. In Sect. 4 the results are presented and in Sect. 5 these results are discussed. We close with our conclusions in Sect. 6.

2. Observations

The observations were conducted during June 1994 using the SEST on La Silla in Chile. The $J = 4 - 3$ transition of HCO^+ at 356734.49 MHz was observed by means of a 0.8 mm SIS receiver which was operated in the frequency switching mode with a throw of 21 MHz. The spectrometer used was a high

Send offprint requests to: Moray Anderson (moray@ceres.helsinki.fi)

⋆ Based on observations collected at the European Southern Observatory, La Silla, Chile

resolution, 2000 channel AOS with an 86 MHz bandwidth and a resolution of 80 kHz. The single sideband receiver temperature was typically ∼350 K. The half-power beam width and the main beam efficiency of the telecope at the frequency observed are 15″ and 0.25, respectively.

Calibration was achieved by the chopperwheel method and was checked by measuring CO($J = 3 - 2$) emission at 345795.975 MHz towards the circumstellar envelope of IRAS 15194-5115. This evolved star was also used for pointing and focusing. We estimate the relative pointing accuracy to be 5″. The absolute pointing is discussed in Sect. 5.

The weather conditions during the run were good and IRS 7 was observed only at elevations above 50°. The atmospheric opacity and the system temperature were in the range 0.45 to 0.9 and 700 K to 1400 K, respectively.

A region 60″ × 60″ was mapped with a 12″ spacing amounting to 56 observation points in total. The map was centred on IRS 7 ($\alpha_{1950.0} = 18^h58^m33\overset{s}{.}0$, $\delta_{1950.0} = -37°01'43''$) and was tilted by 45° with respect to the α and δ axes.

3. Analysis

All of the observed spectra are shown in Fig. 1. It is evident that there are substantial self-absorption features present in many of the spectra located to the south of IRS 7. This immediately complicates the analysis as can readily be appreciated from the HCO$^+$($J = 4 - 3$) integrated intensity map shown in Fig. 2. The disk-like structure which was so apparent in the HCO$^+$($J = 3 - 2$) integrated intensity map (see Paper I, Fig. 6) is not nearly as discernible in the HCO$^+$($J = 4-3$) integrated intensity map. Rather than the principal integrated intensity maxima being located symmetrically either side of IRS 7 as previously, the maximum is now located towards IRS 7 itself.

Attempts to fit the spectra located to the south of IRS 7 with two positive Gaussian components proved to be unsatisfactory. A much better fit was obtained by superposing a positive and a negative Gaussian. This suggests the presence of strong foreground absorption due to an excitation temperature gradient along the line of sight. However, the assumption that the lines are Gaussian may not always be justified so a more rigorous treatment, based on the model outlined below, was employed.

Consider two contacting plane parallel homogeneous layers at different excitation temperatures. Let the excitation temperature of the background and foreground layers be T_1 and T_2, respectively. In what follows all the physical parameters associated with the background layer are denoted by the suffix 1 and those parameters associated with the foreground layer are denoted by the suffix 2. If it is assumed that a) LTE holds in each layer; b) the effect of scattering is negligible; c) the continuum radiation incident upon the rearmost surface of the background layer is Planckian with a temperature $T_{\rm bg}$ and d) the background continuum level changes little over a typical linewidth, then it can readily be shown that the measured antenna temperature T_A^*, as a function of radial velocity v, is given by

$$T_A^*(v) \;=\; \eta\, T_0\, \{[F(T_1) - F(T_{\rm bg})](1 - e^{-\tau_1(v)})e^{-\tau_2(v)} + [F(T_2) - F(T_{\rm bg})](1 - e^{-\tau_2(v)})\}\,, \quad (1)$$

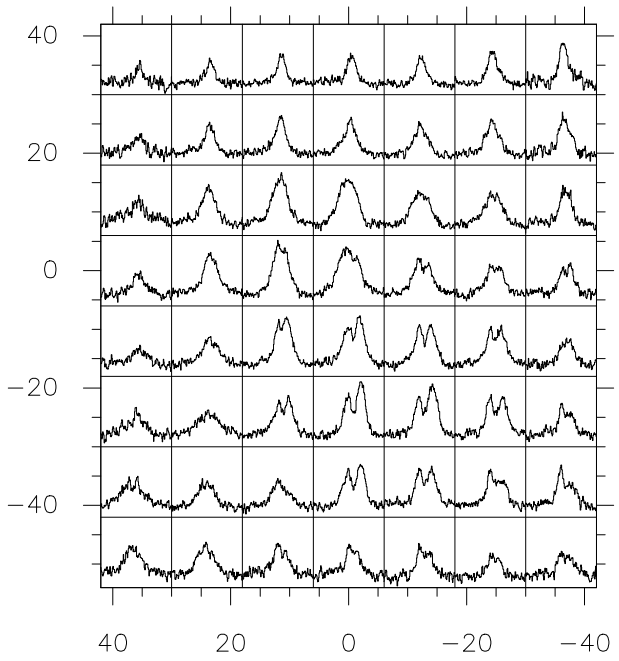

Fig. 1. The HCO$^+$($J = 4 - 3$) spectra. The map is centred on IRS 7. Note that the map has been rotated clockwise through 45° such that NW is up and NE is left. The velocity range and antenna temperature range for each of the spectra is $0 \rightarrow 10\,{\rm km\,s^{-1}}$ and $-1 \rightarrow 5$ K, respectively.

where η is the source-beam coupling efficiency, $T_0 \equiv h\nu_0/k$ with ν_0 the rest-frame frequency of the HCO$^+$($J = 4 - 3$) transition, $T_{\rm bg}$ is the (cosmic) background radiation temperature, and τ_1 and τ_2 are the optical thicknesses of the background and foreground layers, respectively. The function $F(T)$ is defined according to

$$F(T) \equiv \frac{1}{e^{T_0/T} - 1}\,. \quad (2)$$

By making the further definitions

$$T^*_{A_i}(v_{0i}) \equiv \eta\, T_0\, \{F(T_i) - F(T_{bg})\}\, \{1 - e^{-\tau_{0i}}\}, \quad i = 1, 2 \quad (3)$$

the antenna equation may alternatively be expressed as

$$T_A^*(v) \;=\; T^*_{A_1}(v_{01}) \left(\frac{1 - e^{-\tau_1(v)}}{1 - e^{-\tau_{01}}}\right) e^{-\tau_2(v)} + T^*_{A_2}(v_{02}) \left(\frac{1 - e^{-\tau_2(v)}}{1 - e^{-\tau_{02}}}\right)\,. \quad (4)$$

Physically $T^*_{A_1}(v_{01})$ is the line centre antenna temperature which would be observed in the absence of the foreground layer whilst $T^*_{A_2}(v_{02})$ is the line centre antenna temperature which would be observed in the absence of the background layer.

The functional form for the optical depths $\tau_1(v)$ and $\tau_2(v)$ in Eq. (4) is general. For our calculations we assumed that the

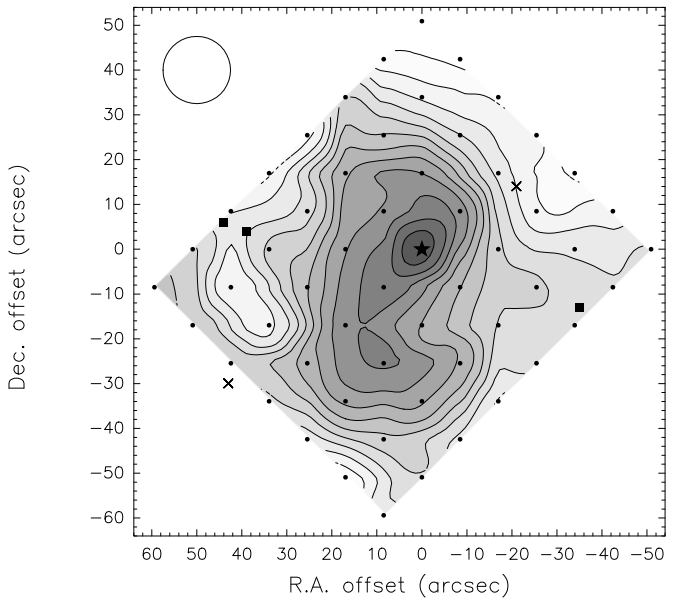

Fig. 2. The integrated intensity of HCO$^+$(J = 4 − 3) emission in the LSR velocity range $0 \rightarrow 10\,\mathrm{km\,s^{-1}}$. The contour levels are from $3 \rightarrow 14\,\mathrm{K\,km\,s^{-1}}$ in increments of $1\,\mathrm{K\,km\,s^{-1}}$. The position of IRS 7 is marked by a star. The locations of R CrA (right) and T CrA (left) are marked by crosses whilst the locations of HH104A & B (left) and HH98 (right) are marked by squares. The beamsize is indicated in the top left of the figure.

intrinsic line profile shape is Gaussian and, therefore, the optical depth may be expressed as

$$\tau_i(v) = \tau_{0i} \exp\left\{-\frac{4\ln 2\,(v - v_{0i})^2}{\Delta v_i^2}\right\} \quad i = 1, 2\ , \tag{5}$$

where τ_{0i} is the line centre opacity, v_{0i} is the line centre velocity and Δv_i is the intrinsic FWHM. The observed FWHM is related to the intrinsic line width and the line centre opacity by e.g. Eq. (3) in Phillips et al. (1979).

To appreciate the nature of the antenna temperature equation consider the simplified scenario in which the peak optical depth of each layer along the line of sight occurs at the same velocity, v_0. At this velocity Eq. (4) then reduces to

$$T_A^*(v_0) = T_{A_1}^*(v_0)\, e^{-\tau_{02}} + T_{A_2}^*(v_0)\,. \tag{6}$$

For the foreground layer to produce an absorption feature in the observed spectral line, the inequality $T_A^*(v_0) < T_{A_1}^*(v_0)$ needs be satisfied. By Eq. (6), this requires that

$$T_{A_1}^*(v_0) > \frac{T_{A_2}^*(v_0)}{1 - e^{-\tau_{02}}}\ . \tag{7}$$

Evidently, if both $T_{A_1}^*(v_0)$ and $T_{A_2}^*(v_0)$ are positive, this condition is more likely to be satisfied when the foreground layer is optically thick rather than when it is optically thin. Note, however, that the inequality will always be satisfied, masering effects excluded, when $T_{A_1}^*(v_0) > 0$ and $T_{A_2}^*(v_0) \leq 0$. By Eqs. (2) and (3), this necessitates that $T_2 \leq T_{\mathrm{bg}} < T_1$. Such an outcome is possible if the source of the background radiation is other than the cosmic background. This is conceivable nearby IRS 7 as the region is a known source of continuum radiation (e.g. Brown 1987 and Henning et al. 1994).

As the background and foreground layers may be either optically thin or optically thick, there are 4 possible optical depth combinations and each needs be considered:

1) Background optically thick, foreground optically thick
The antenna equation is prescribed by Eq. (4) with the optical depth given by Eq. (5). There are 8 free parameters in total: $T_{A_1}^*(v_{01})$, τ_{01}, v_{01}, Δv_1, $T_{A_2}^*(v_{02})$, τ_{02}, v_{02} and Δv_2.

2) Background optically thin, foreground optically thick
The antenna equation becomes

$$T_A^*(v) \;=\; T_{A_1}^*(v_{01}) \exp\left\{-\frac{4\ln 2\,(v - v_{01})^2}{\Delta v_1^2} - \tau_2(v)\right\} + T_{A_2}^*(v_{02})\left(\frac{1 - e^{-\tau_2(v)}}{1 - e^{-\tau_{02}}}\right)\ . \tag{8}$$

There are 7 free paramaters, τ_{01} having become redundant.

3) Background optically thick, foreground optically thin
The antenna equation becomes

$$T_A^*(v) = T_{A_1}^*(v_{01})\left(\frac{1 - e^{-\tau_1(v)}}{1 - e^{-\tau_{01}}}\right) + T_{A_2}^*(v_{02})\, e^{-\frac{4\ln 2\,(v - v_{02})^2}{\Delta v_2^2}}\ . \tag{9}$$

There are 7 free parameters, τ_{02} having become redundant.

4) Background optically thin, foreground optically thin
The antenna equation becomes

$$T_A^*(v) = T_{A_1}^*(v_{01}) e^{-\frac{4\ln 2\,(v - v_{01})^2}{\Delta v_1^2}} + T_{A_2}^*(v_{02}) e^{-\frac{4\ln 2\,(v - v_{02})^2}{\Delta v_2^2}}\ . \tag{10}$$

There are 6 free parameters, τ_{01} and τ_{02} having become redundant. From Eq. (10) it can be seen that the oft-employed method of subtracting one Gaussian line from another to model a line exhibiting self-absorption can be physically realised only when $T_{A_2}^*(v_{02}) < 0$ i.e. when $T_2 < T_{\mathrm{bg}}$.

For those lines exhibiting an absorption feature a least squares fit to each of the 4 possible combinations above was made. Each fit was scrutinised by eye and those with implausible parameter values were excluded. Of those that remained, the selected fit was that with the lowest X^2. For those lines which did not have an absorption feature both an optically thin (3 free parameters) and an optically thick (4 free parameters) single profile fit was made. Again, the parameter values chosen were those which gave the lowest X^2. A montage of 4 typical line profiles and their best fits is shown in Fig. 3.

4. Results

From inspection of the line profiles in Fig. 1 it can be appreciated that, if the regions surrounding an absorption feature are ignored, none of the spectra exhibit gross asymmetries about a central velocity axis. Thus, although the central part of the

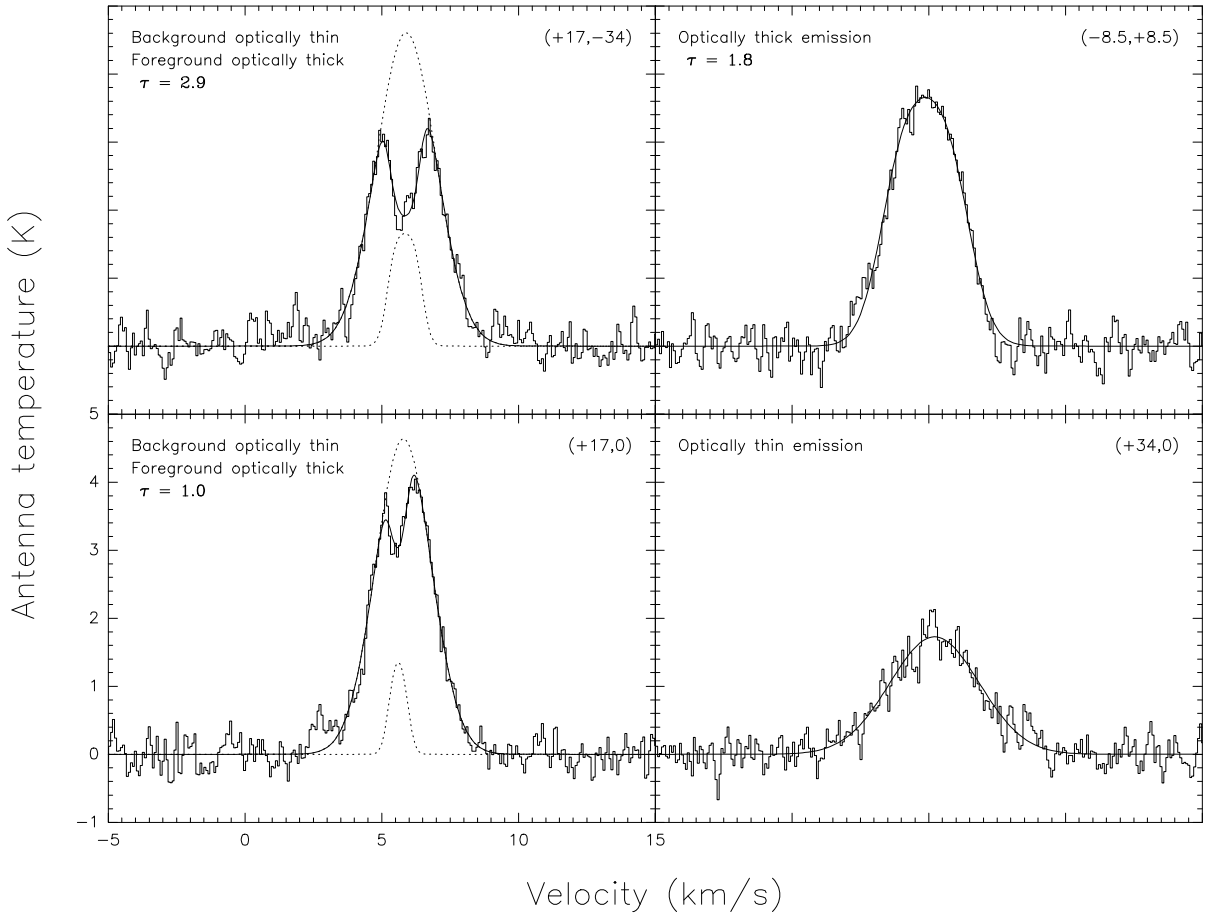

Fig. 3. Representative spectra and their best fits. The offset of each spectrum, in arcseconds from IRS 7, is given in the top right of each frame. The full lines represent the fit to the observed spectrum whilst the dotted lines denote the emission (background layer) and absorption (foreground layer) line profiles. The adopted upper bound for optically thin emission is 0.01.

spectrum may be 'contaminated' by an absorption feature it is possible to determine the line centre velocity v_{01} with considerable confidence. The same reasoning can also be applied to the determination of the line centre velocity, v_{02}, of the absorption line profile. However, for the remaining line parameters there is no such symmetry check so their derived values must be treated with a good deal more caution. Consequently, we concentrate on the results which can be derived from the line centre velocities.

The radial velocity distribution of the emission line component is shown in Fig. 4. To the northwest of IRS 7 there is a compact, elongated region of blueshifted emission whilst to the south and southwest of IRS 7 there is a more extended region of redshifted emission. The former feature, which is localized around the offset $(-8.5'', +8.5'')$, is coincident, within pointing uncertainties, with the approaching side of the molecular disk detected in the previous HCO$^+$(J = 3 − 2) survey (Paper I). The most redshifted material, located towards the offset $(8.5'', -25.5'')$, is coincident with what was termed the 'southern extension' in Paper I. The source of this emission was postulated as being a stream of gas flowing from the dense, foreground core to the receding side of the molecular disk. The region towards the offset $(+12'', -4'')$ is strongly redshifted though there is no clearly delineated counterpart to the redshifted side of the molecular disk that was observed in HCO$^+$(J = 3 − 2) (see Fig. 6 in Paper I).

For comparitive purposes the HCO$^+$(J = 3 − 2) line centre velocity, determined by precisely the same method as was employed for the HCO$^+$(J = 4 − 3) data, is shown in Fig. 5. Though the spatial resolution is slightly poorer on account of the larger beamsize, there is considerably less evidence of the disk's structure than can be explained by this fact alone. Possible reasons for this are, firstly, that as the critical density for the HCO$^+$(J = 4 − 3) transition is $\sim 3 \times 10^7$ cm^{-3}, roughly 3 times that for the J = 3 − 2 transition[1], the J = 4 − 3 emission better traces the velocity extrema close to the central protostar, IRS 7. A second possible explanation lies with the foreground material located southward of IRS 7. Since there is strong HCO$^+$(J = 3 − 4) absorption in this region there will also be strong J = 3 − 2 emission. Though this emission is not

[1] These critical densities are obtained by using a dipole moment of 4.48 D from Haese & Woods (1979) and collisional rates from Green (1975).

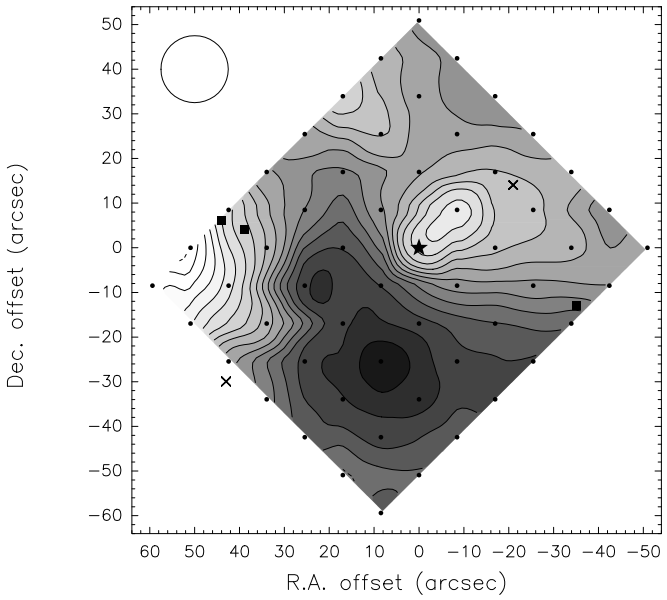

Fig. 4. The line centre velocity of the HCO$^+$(J = 4 − 3) emission line component. The light regions represent blueshifted gas whilst the dark regions represent redshifted gas. The contour levels are from 4.4 → 6.0 km s^{-1} in increments of 0.1 km s^{-1}. The markers have the same significance as in Fig. 2.The beamsize is indicated in the top left of the figure.

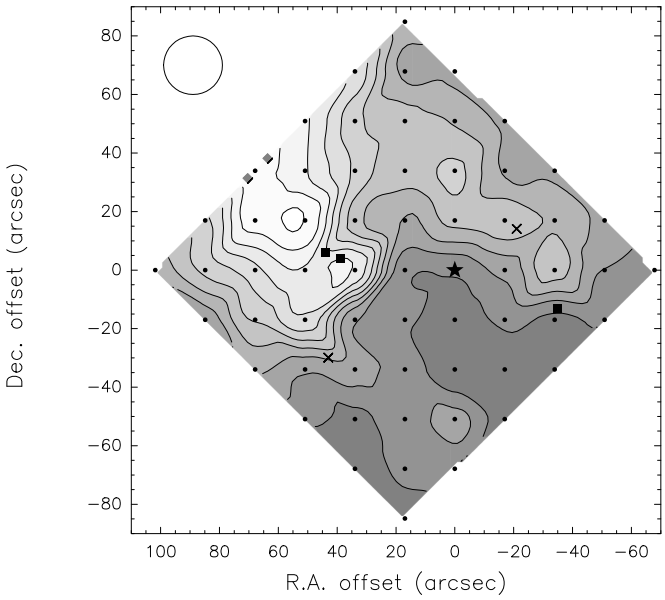

Fig. 5. The line centre velocity of the HCO$^+$(J = 3 − 2) emission line component. The light regions represent blueshifted gas whilst the dark regions represent redshifted gas. The contour levels are from 3.8 → 5.6 km s^{-1} in increments of 0.2 km s^{-1}. The markers have the same significance as in Fig. 2. The beamsize is indicated in the top left of the figure. The data are from Paper I.

strong enough to noticeably affect the total integrated line intensity it may have the effect of smoothing out velocity gradients in the region by forcing the line peak velocity towards that of the foreground material.

A statistical analysis of the line centre velocity of a sample of 16 spectra exhibiting clearly defined absorption profiles shows that the mean velocity of the foreground layer is 5.7 km s^{-1} with a standard deviation of 0.1 km s^{-1} whilst the mean intrinsic and observed FWHM of the profiles are 0.8 km s^{-1} and 1.1 km s^{-1} with standard deviations of 0.3 km s^{-1} and 0.1 km s^{-1}, respectively. The typical central velocity of the HCO$^+$(J = 3 − 2) emission south of IRS 7 (see Fig. 5) is in the velocity range 5.6 → 5.8 km s^{-1} which is comparable to the typical velocity of the foreground layer. This supports the latter notion above.

Although there are noticeable differences between the velocity contour maps presented in Figs. 4 and 5 they do, however, exhibit the same large scale velocity gradients. Furthermore, the blueshifted outflow, which originates from somewhere close to IRS 7, is clearly defined in both maps towards the Herbig-Haro objects HH104A & B eastward of IRS 7.

5. Discussion

The absorption features are markedly deeper in the HCO$^+$(J = 4 − 3) spectra then in the J = 3 − 2 spectra indicating that the optical thickness of the J = 4 − 3 transition is higher than that for J = 3 − 2. In LTE the optical thickness ratio of two transitions $u \rightarrow u-1$ and $l \rightarrow l-1$, as a function of the excitation temperature $T_{\rm ex}$, is approximately

$$\frac{\tau_{u\rightarrow u-1}}{\tau_{l\rightarrow l-1}} \approx \frac{J_u}{J_l} e^{-[J_u(J_u+1)-J_l(J_l+1)]E_1/(2T_{\rm ex})} \frac{e^{J_u E_1/T_{\rm ex}}-1}{e^{J_l E_1/T_{\rm ex}}-1}\,, \quad (11)$$

where $E_1 \equiv h\nu_{10}/k$ equals 4.28 K for the HCO$^+$ molecule. Specifically, for the J = 4 − 3 and J = 3 − 2 transitions the optical depth ratio is given by

$$\frac{\tau_{4\rightarrow 3}}{\tau_{3\rightarrow 2}} \approx \frac{4}{3} e^{-4E_1/T_{\rm ex}} \frac{e^{4E_1/T_{\rm ex}}-1}{e^{3E_1/T_{\rm ex}}-1}\,. \quad (12)$$

This ratio exceeds unity when $T_{\rm ex}$ is greater than about 26 K. This implies that the gas responsible for the J = 3−4 absorption feature is relatively warm.

From inspection of Figs. 1 and 4 it can be discerned that those spectra which exhibit the strongest self-absorption features lie towards the redshifted side of the molecular disk and towards the redshifted southern extension, termed the accretion stream in Paper I. The presence of a shock in this region, most likely attributable to accretion, is suggested by the detection of SiO(J = 2 − 1, v = 0) emission, as presented in Paper I. The relatively warm gas causing the self-absorption features may be heated by the accretion shock. An alternative heating mechanism is ionization and subsequent heating due to X-rays produced by magnetic field activity (Montmerle et al. 1993) close to the surface of IRS 7.

For the HCO$^+$(J = 4 − 3) spectra which exhibit strong self-absorption features, the line centre velocity and FWHM of the

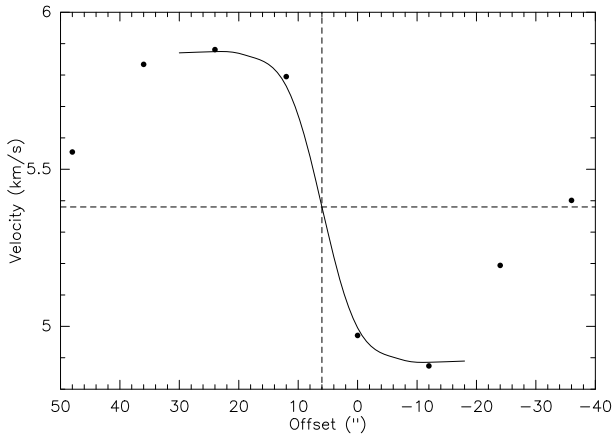

Fig. 6. The line centre velocity of the HCO$^+$(J = 4 − 3) emission line spectra along a strip with position angle 135° passing through IRS 7. The intersection of the dashed lines marks the antisymmetry centre of the inner four points whilst the full line denotes a model fit to the same four data points. Details of the model are given in the text.

H^{13}CO$^+$(J = 1 − 0) emission are 5.5 km s^{-1} and 1.1 km s^{-1}, respectively. These values are comparable to those for the HCO$^+$(J = 4 − 3) absorption profiles indicating that the self–absorption features are probably caused by the dense, quiescent foreground core mapped in Paper I. The density of the foreground core can be somewhat lower than the critical density of the HCO$^+$(J = 4 − 3) transition if it is optically thick.

Failure of the HCO$^+$(J = 4 − 3) observations presented in Fig. 4 to resolve the redshifted side of the molecular disk can be attributed to the low velocity dispersion between the southern extension and the redshifted side of the disk. From the previous HCO$^+$(J = 3 − 2) observations detailed in Paper I, the velocity dispersion was found to range approximately from 1 → 2.5 km s^{-1}. As Fig. 4 maps the velocity, rather than the integrated intensity as in Fig. 6 of Paper I, this low velocity dispersion between the redshifted features results in their being unresolved. The redshifted region to the northeast of the southern extension can, therefore, be ascribed to the redshifted side of the molecular disk.

An estimate for the mass of the central protostar can obtained from the NW-SE directed velocity gradient. The line centre velocities of the emission line component along the strip with position angle 135° passing through IRS 7 are plotted in Fig. 6. The intersection of the dashed lines marks the antisymmetry centre of the inner four points and is located at an offset of 6″ and $v_{\rm LSR}$ = 5.38 km s^{-1}. The outer four data points approach the average LSR velocity of the cloud.

From the data presented in Fig. 4 it can be deduced that the semi-angular size of the disk is between ∼ 18″ and ∼ 30″. This corresponds to a physical radius of between 2 300 and 3 900 AU at an assumed distance of 130 pc (Marraco & Rydgren 1981). This bound on the disk's radius is consistent with that derived from the HCO$^+$(J = 3 − 2) data presented in Paper I.

In order to estimate the mass of the central protostar the line profiles towards an edge–on Keplerian disk were calculated in the same manner as described in Paper I (Sect. 6.3). The outer radius, $R_{\rm out}$, was assumed to extend out to 3 000 AU or 24″ from the central protostar. The disk was assumed to be isothermal. The best fit to the observed velocity pattern close to IRS 7 was obtained by setting the central mass to 0.8 M$_\odot$, the inner radius to 0.1 $R_{\rm out}$ and the density power law to $n(r) = n_{\rm out}\, r^{-2}$. The peak velocities resulting from Gaussian fits to these modelled spectra are presented as the full curve in Fig. 6. As the disk was assumed to be edge–on, the figure of 0.8 M$_\odot$ represents a lower bound to the mass of the central protostar.

The LSR velocity of 5.38 km s^{-1} derived from the HCO$^+$(J = 4 − 3) data is close to the value of 5.30 km s^{-1} obtained from the C^{18}O(J = 2 − 1) data in Paper I. However, the positions of the spatial asymmetry centres are quite different. The position offset derived from the the C^{18}O(J = 2 − 1) Gaussian velocity data was about −6″.

The 12″ separation between the antisymmetry centres derived from the HCO$^+$(J = 4 − 3) and C^{18}O(J = 2 − 1) data is large and cannot be understood entirely in terms of the different physical conditions traced by these transitions. It should be noted, however, that the absolute pointing of the HCO(J = 4−3) data is less accurate than for the earlier 1.3 mm observations due to the absence of suitable 0.8 mm pointing sources in the neighbourhood of IRS 7. Therefore, the HCO(J = 4 − 3) map may be shifted by ∼ 6 − 12″ to the northwest with respect to the fixed markers. Such a shift would also bring the Herbig-Haro objects HH104 A & B closer to the blueshifted outflow maximum on the eastern edge of the map.

6. Conclusions

The present HCO$^+$(J = 4 − 3) observations augment our previous study of the dense molecular gas component near IRS 7.

The location of the blue and redshifted HCO$^+$(J = 4 − 3) emission correlates well with the location of similarly Doppler shifted HCO$^+$(J = 3 − 2) emission: the molecular disk, the southern extension and the blueshifted outflow.

The HCO$^+$(J = 4 − 3) data provide confirmation of the low velocity dispersion between the redshifted side of the molecular disk and the southern extension. This supports the notion that the southern extension is physically connected to the receding side of the molecular disk and does not represent outflow from the central source. The presence of the strong self-absorption features in the spectra southward of IRS 7 confirms the presence of a dense foreground core in the direction of the southern extension.

The velocities of the HCO$^+$(J = 4−3) emission lines display an antisymmetric pattern along the molecular disk axis. The position of the antisymmetry centre is not coincident with IRS 7 and it is different from the location derived in our previous study, although the central velocity is roughly the same. We suggest the discrepancy between the locations can be attributed uncertainties in the pointing.

Assuming that the molecular disk is Keplerian and viewed edge on, an estimate of 0.8 M$_\odot$ for the mass of the central object is obtained. This mass is consistent with the lower limit of

$0.6\,M_\odot$ derived from the earlier $HCO^+(J = 3 - 2)$ measurements.

Acknowledgements. The Swedish–ESO Submillimetre Telescope, SEST, is operated jointly by ESO and the Swedish National Facility for Radio Astronomy, Onsala Space Observatory at Chalmers University of Technology.

References

Anderson I.M., Harju J., Knee L.B.G., Haikala L.K. 1997, A&A 321, 575 (Paper I)
André P., Montmerle T., 1994, ApJ 420, 837
Brown A., 1987, ApJ 322, L31
Casanova S., Montmerle T., Feigelson E.D., Andeé P., 1995, ApJ 439, 752
Green S. 1975, ApJ 201, 366
Haese N.N., Woods R.C., 1979, Chem. Phys. Lett. 61, 396
Henning Th., Launhardt R., Steinacker J., Thamm E., 1994, A&A 291,546
Koyama K., Hamaguchi K., Ueno S., Kobayashi N., Feigelson E., 1996, Publ. Astron. Soc. Japan 48, L87
Lada C.J., 1987, in Proc. IAU Symp. 115, Star Forming Regions, ed. M. Peimbert & J. Jugaku, pub. D. Reidel
Marraco H.G., Rydgren A.E., 1981, AJ 86, 62
Montmerle T., Feigelson E.D., Bouvier J., André P., 1993, in Protostars and Planets III, ed. E.H. Levy & J.I. Lunine, pub. The University of Arizona Press
Phillips T.G., Huggins P.J., Wannier P.G., Scoville N.Z., 1979, ApJ 231, 720
Taylor K.N.R., Storey J.W.V., 1984, MNRAS 209, 5P
Wilking B.A., Taylor K.N.R., Storey J.W.V., 1986, AJ 92, 103

This article was processed by the author using Springer-Verlag LaTeX A&A style file *L-AA* version 3.